Domain Collisions

Yago Bea,[1] Jorge Casalderrey-Solana,[2] Thanasis Giannakopoulos,[3]
David Mateos,[2,4] Mikel Sanchez-Garitaonandia,[2] and Miguel Zilhão[3]

[1] Department of Physics and Helsinki Institute of Physics, PL 64, FI-00014 University of
Helsinki, Finland.

[2] Departament de Física Quántica i Astrofísica and Institut de Ciències del Cosmos (ICC),
Universitat de Barcelona, Martí i Franquès 1, ES-08028, Barcelona, Spain.

[3] Centro de Astrofísica e Gravitação (CENTRA),
Departamento de Física, Instituto Superior Técnico, Universidade de Lisboa,
Av. Rovisco Pais 1, 1049-001 Lisboa, Portugal.

[4] Institució Catalana de Recerca i Estudis Avançats (ICREA),
Passeig Lluís Companys 23, ES-08010, Barcelona, Spain.

Abstract

We use holography to study collisions of phase domains formed in a four-dimensional,
strongly-coupled gauge theory with a first-order, thermal phase transition. We find three
qualitatively different dynamical regimes depending on the collision velocity. For low
velocities the domains slow down before the collision and subsequently merge and relax to
equilibrium. For intermediate velocities no slow down is present before the merger. For
high enough velocities the domains can collide and break apart several times before they
finally merge. These features leave an imprint on the time evolution of the entropy of the
system, which we compute from the area of the dual horizon on the gravity side.

Contents

1 Introduction

Holography has provided numerous insights into the out-of-equilibrium properties of hot, strongly-coupled, non-Abelian plasmas [1–32] (see e.g. [33] for a review). Here we will apply it to a four-dimensional gauge theory with a first-order, thermal phase transition. Imagine placing the theory in an initial homogeneous state with an energy density in the unstable, spinodal region (see Fig. 1). If this state is perturbed, the system will evolve to a final state that will necessarily be inhomogeneous. Following this real-time evolution with conventional quantum-field theoretical methods for an interacting gauge theory is challenging. For this reason, Refs. [18–20] used holography, i.e. they followed the evolution by solving the time-dependent Einstein's equations on the gravity side. The evolution consists of four generic stages [20] visible in Fig. 2: A first, linear stage in which the instability grows exponentially; a second, non-linear stage in which peaks and/or phase domains are formed; a third stage in which these structures collide and merge; and a fourth stage in which the system finally relaxes to a static, phase-separated configuration. In any given evolution of this type, the velocities of the different domains are a complicated function of the perturbation of the initial, homogeneous state. This makes it difficult to perform a systematic study of the physics of the collision as a function of the domain velocities. In this paper we will overcome this difficulty by directly preparing initial states consisting of domains moving towards each other at a wide range of velocities.

On the gravity side the above dynamics translates into the physics of a time-dependent, inhomogeneous horizon. Understanding this physics provides one motivation for our work. For example, we will examine in detail how the area of the horizon changes as two domains merge. Another motivation comes from heavy ion collision (HIC) experiments such as the beam energy scan at RHIC, the compressed baryonic matter experiment at FAIR and other experiments at NICA. These experiments will open an unprecedented window into the properties of the phase diagram of Quantum Chromodynamics (QCD) at large baryon chemical potential, which is expected to contain a line of first order phase transitions ending at a critical point [34–36]. If this scenario is realised then the real-time dynamics of the spinodal instability may play an important role.

One technical aspect that will allow us to go significantly beyond [18, 20] is our choice of scalar potential on the gravity side. The choice in those references gave rise to a phase
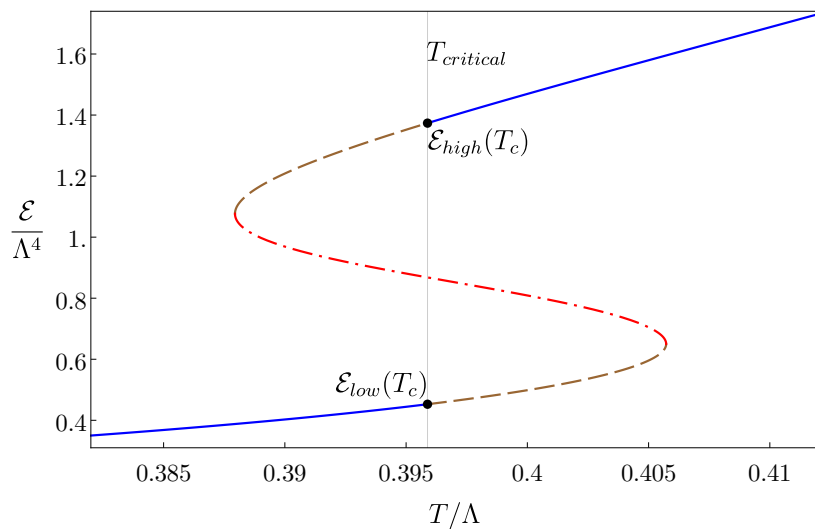
Figure 1: Energy as a function of temperature for the theory considered in this paper, with intrinsic scale Λ. Stable, metastable and unstable states are represented by solid, dashed and dot-dashed curves, respectively. The vertical grey line corresponds to the phase transition temperature.
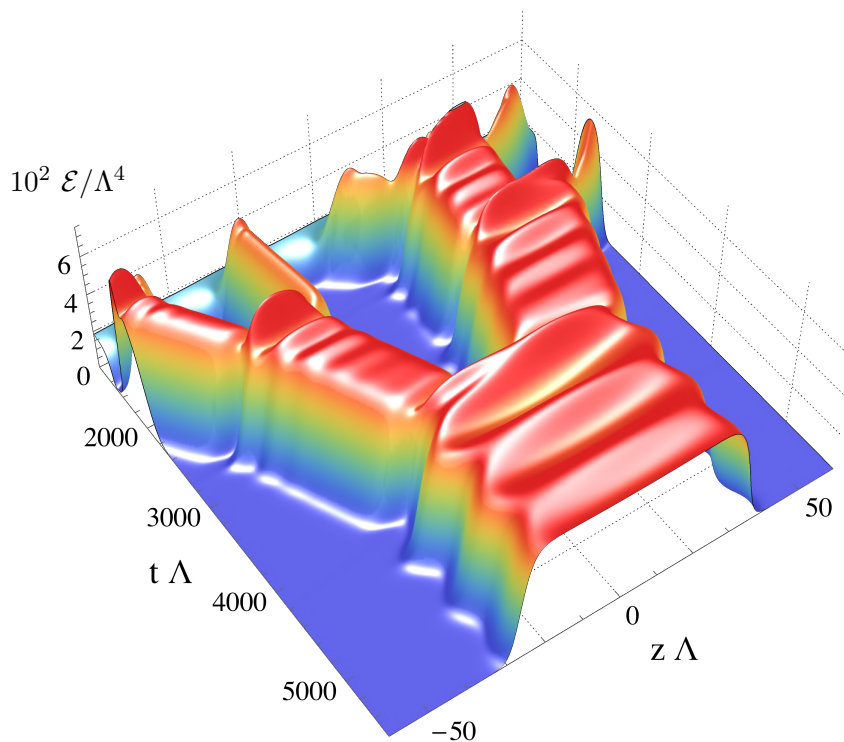

Figure 2: Evolution of the energy density as a function of time and space for an initial homogeneous state in the spinodal region that is slightly perturbed at $t = 0$. Figure taken from [20].

diagram in the gauge theory with a large hierarchy between $\mathcal{E}_{high}$ and $\mathcal{E}_{low}$. This large ratio resulted in a run-time for our code on the scale of months. In contrast, here we will use

2

the potential introduced in [37] and subsequently used in [29, 31]. With this choice the ratio $\mathcal{E}_{high}/\mathcal{E}_{low}$ is of order one and the run-time decreases to minutes.

We emphasize from the start that the domains we consider here should not be confused with the bubbles created via a nucleation process in first-order phase transitions. The expansion of those bubbles is driven by a pressure difference between the inside and the outside of the bubble. Instead, in our case the domains move simply because they are created with some initial velocity. In fact, if a number of bubbles are nucleated in a large – but finite-size – box, and if the average energy density in the box is between $\mathcal{E}_{high}$ and $\mathcal{E}_{low}$, then the endpoint of the evolution will be a phase-separated state with two domains with energies $\mathcal{E}_{high}$ and $\mathcal{E}_{low}$.

2   The model

Our gravity model is described by the Einstein-scalar action

$$S = \frac{2}{\kappa_5^2} \int d^5 x \sqrt{-g} \left[\frac{1}{4} \mathcal{R} - \frac{1}{2} (\nabla \phi)^2 - V(\phi) \right] . \qquad (2.1)$$

Exclusively for simplicity we assume that the scalar potential $V(\phi)$ can be derived from a superpotential $W(\phi)$ through the usual relation

$$V(\phi) = -\frac{4}{3} W(\phi)^2 + \frac{1}{2} W'(\phi)^2 . \qquad (2.2)$$

Different choices of (super)potential correspond to different dual four-dimensional gauge theories. As in [29, 31, 37] we choose

$$\ell W(\phi) = -\frac{3}{2} - \frac{\phi^2}{2} - \frac{\phi^4}{4\phi_M^2} + \frac{\phi^6}{\phi_Q} , \qquad (2.3)$$

where ℓ is the asymptotic curvature radius of the corresponding AdS geometry and ϕ_M, ϕ_Q are constants, which in this paper we will set to $\phi_M = 1.0$ and $\phi_Q = 10$. The dual gauge theory is a conformal field theory (CFT) deformed with a dimension-three scalar operator with source Λ. This intrinsic scale in the gauge theory will set the characteristic scale of much of the physics of interest. On the gravity side, Λ appears as a boundary condition for the scalar ϕ. In the limit $\phi_Q \to \infty$ the sextic term is absent and the model reduces to that in [18, 20, 27]. The motivation for the choice here is simplicity: the dual gauge theory is a non-conformal theory with a first-order phase transition with a ratio $\mathcal{E}_{high}/\mathcal{E}_{low}$ of order one, as shown in Fig. 1, and the dual gravity solution is completely regular even at zero temperature. This model has $T_{critical}/\Lambda = 0.3959$, $\mathcal{P}_{critical}/\Lambda^4 = 0.1124$, $\mathcal{E}_{high}/\Lambda^4 = 1.3736$ and $\mathcal{E}_{low}/\Lambda^4 = 0.4526$.

For simplicity, in this paper we will allow for dynamics only along one of the three spatial directions of the gauge theory, which we call z. In other words, we impose translational symmetry along x, y. We will also refer to z as the longitudinal coordinate and to x, y as the transverse directions. We will decompose the gauge theory stress tensor accordingly and work with the rescaled quantities

$$(\mathcal{E}, P_T, P_T, P_L, \mathcal{J}) = \frac{\kappa_5^2}{2\ell^3} (-T_t^t, T_x^x, T_y^y, T_z^z, T_z^t), \qquad (2.4)$$

where $\mathcal{E}$ is the energy density, P_L and P_T are the longitudinal and transverse pressures, and $\mathcal{J}$ is the momentum density in the z-direction. For an $SU(N_c)$ gauge theory the prefactor

on the right-hand side typically scales as N_c^{-2}. In addition, we compactify the z-direction on a circle of length L. This infrared cut-off is technically convenient since it reduces the number of unstable modes of homogeneous states in the spinodal region to a finite number. In addition, compactifying the z-direction on a circle also brings about interesting new effects even for a single, boosted domain. We will start by analyzing this case in Sec. 3 and then we will move to collisions of two domains in Sec. 4. Note that we are slightly abusing the word "domain" in the following sense. At the end of the evolution in Fig. 2 there are two domains with energy densities $\mathcal{E}_{high}$ and $\mathcal{E}_{low}$. Nevertheless, we will often use the word "domain" to refer specifically to the high-density phase. In this sense, we will sometimes think of the end state of Fig. 2 as a domain surrounded by a low-density bath.

3 Domains in motion

In a domain collision, each of the participants is initially moving independently of the other, surrounded by a low-density bath. In this section we will study the dynamics of such a single domain. We will construct an initial, out-of-equilibrium state with a non-uniform fluid velocity in the z-direction and watch it evolve into a steady-state with uniform velocity. In addition to its intrinsic interest, this will also help us understand the construction of initial states in the case of domain collisions.

We start with a single, static domain obtained as the end-state of a simulation like that in Fig. 2. We then modify the near-boundary fall-offs of the metric functions on the initial time slice on the gravity side[1] so as to add a finite momentum density along the z-direction, $\mathcal{J}(z)$. We keep the total energy fixed as we inject this momentum; as we will see below this results in a decrease in the entropy of the system. The specific z-dependence is chosen to be

$$\mathcal{J}(z) = j \left(\mathcal{E}(z) - \mathcal{E}_{low}(T_c) \right), \qquad (3.1)$$

where j is an appropriately chosen constant. At this initial step the momentum density has vanishing support on the low-density region. In order to be able to initialise our numerical code the initial value of j cannot be too large. However, choosing a small value, letting the system evolve for a few time steps, increasing the value of j, and iterating this procedure, allows us to eventually reach high velocities. The reason for the iterations is that, after each change in the near-boundary fall-offs, a few time steps of evolution allow the bulk functions to adapt to the new near-boundary fall-offs. In particular, this allows our code to find the new horizon within our numerical grid. We will define as the initial time, $t\Lambda = 0$, the time at the end of this iterative process. At each step in the iteration process a fraction of the total momentum gets transferred to the low-density bath. As a consequence, at the end of the process the bath will not be completely at rest, as illustrated by the blue curve in Fig. 3(top). Nevertheless, at this time most of the momentum density is still in the domain, where the fluid flow velocity is larger than in the bath. It is precisely this feature that tells us that the resulting state at $t\Lambda = 0$ is out of equilibrium.

After $t\Lambda = 0$ we do not inject any more momentum into the system. The subsequent evolution is characterized by a significant energy and momentum transfer between the domain and the bath. The initial state is so far from equilibrium that it splits into several fragments that eventually merge back to form a single domain, as illustrated in Fig. 4. The stationary state is reached around $t\Lambda \sim 400$. At this and at later times the fluid velocity field is constant along the z-direction with value $v = 0.364$, as seen in Fig. 3(top). In other words, the "system

---

[1]Specifically the subleading terms, which determine the expectation values.
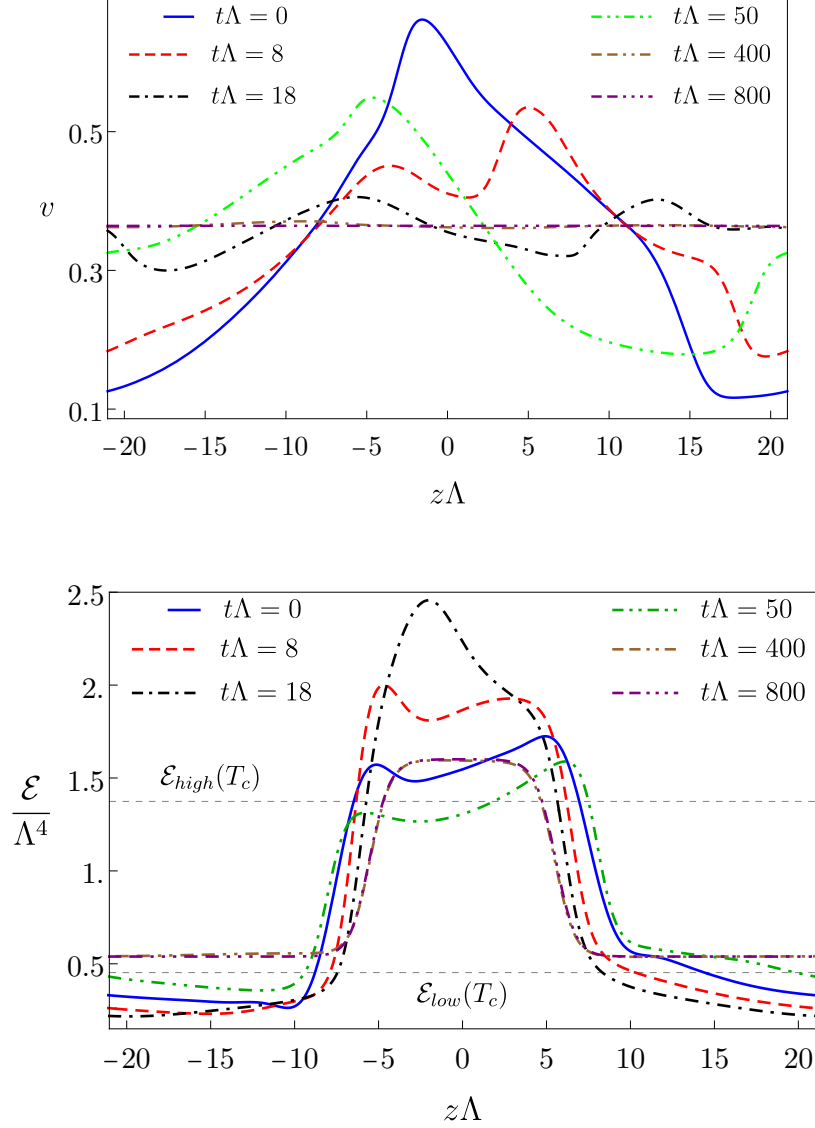
Figure 3: Time evolution of the fluid velocity (top) and of the energy density profile (bottom) for a domain in motion. To facilitate the comparison, each profile has been shifted by a constant amount to match the domain midpoint with $z\Lambda = 0$. The maximum of the fluid velocity at $t\Lambda = 0$ is $v_{max} = 0.66$.

moves as a whole". This is illustrated in Fig. 5, where we see that the energy density profile remains constant in time once the steady state is reached to a precision better than 1%. This steady-state energy profile is narrower than that of the out-of-equilibrium state at $t\Lambda = 0$, as can be seen in Fig. 3(bottom), and it is also narrower than that of the static, equilibrium state with the same total energy, as illustrated in Fig. 6 for two different velocities.

We see in the figure that the domains become narrower as the velocity increases, and that the energy densities in the domain and in the bath are higher than $\mathcal{E}_{high}(T_c)$ and $\mathcal{E}_{low}(T_c)$, respectively. These features are consistent with the fact that, by construction, all these configurations have the same total energy.

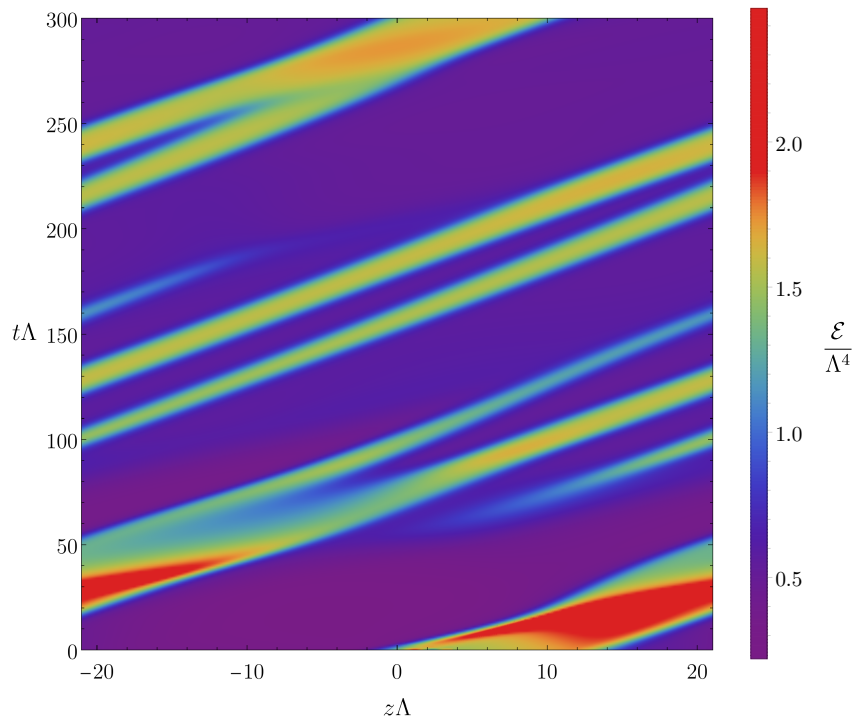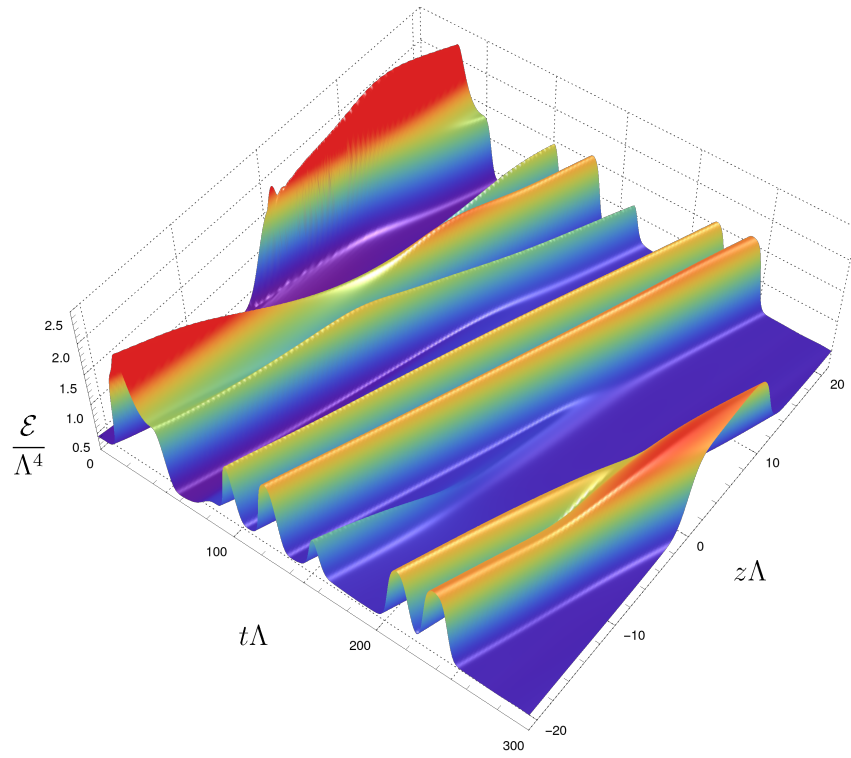In the steady state, a comoving observer traveling with velocity v sees a fluid configura-

5

Figure 4: Plots of the energy density for the evolution of an initial, single-domain state that splits into several fragments that subsequently merge back into a single domain.
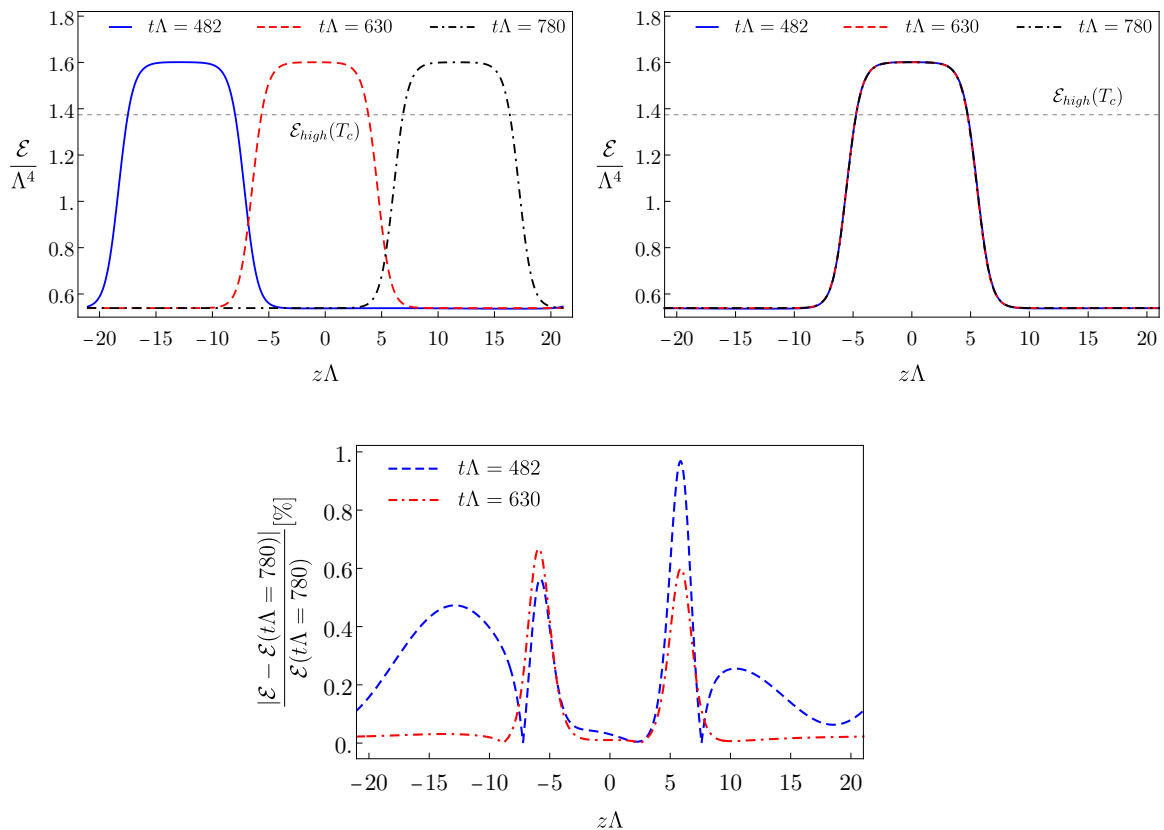
Figure 5: (Left) Snapshots of the energy density at late times for the same initial state as in Fig. 3. (Right) The same profiles shifted by an appropriate constant. (Bottom) Relative difference between the profiles.

tion at rest. This observer uses coordinates t', z' related to t, z through the usual Lorentz transformation

$$t' = \gamma(t - vz), \qquad z' = \gamma(z - vt), \qquad \gamma = (1 - v^2)^{-1/2}. \tag{3.2}$$

The original identification $(t, z) \sim (t, z + L)$, translates into a non-trivial identification for the comoving observer

$$(t', z') \sim (t' - \gamma v L, z' + \gamma L). \tag{3.3}$$

In other words, for the co-moving observer the identification is not purely along the spatial direction but it involves time as well. This imposes a non-trivial constraint on any physical configuration seen by this observer, since any such configuration must be invariant under (3.3). However, for configurations that are static with respect to the comoving observer this condition reduces to periodicity along the z'-direction with period $L' = \gamma L$. This is the case for the fluid configuration obtained by applying the Lorentz transformation (3.2) to the configurations of Fig. 6. In particular, the energy density in the comoving frame takes the form

$$\mathcal{E}' = \gamma^2 \left(\mathcal{E} + v^2 P_z - 2v\mathcal{J} \right), \tag{3.4}$$

and the average energy in this frame is

$$\bar{\mathcal{E}}' = \bar{\mathcal{E}} - v\bar{\mathcal{J}}. \tag{3.5}$$
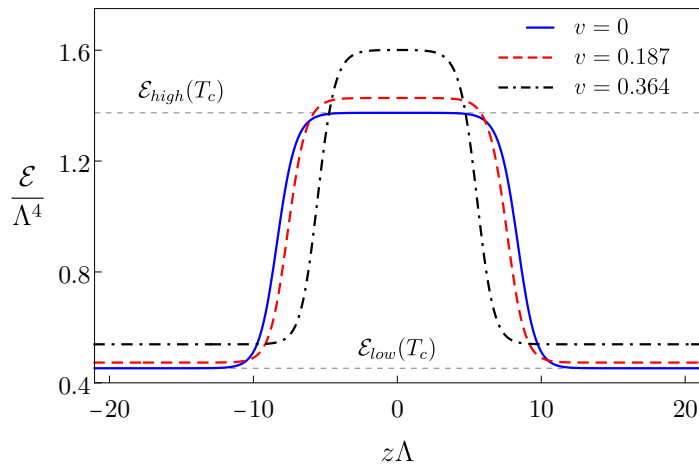
7

Figure 6: Steady-state energy profiles of domains with different velocities. The total energy in the box is the same in all cases. The average energy is $\bar{\mathcal{E}}/\Lambda^4 = 0.817$ and the box has size $L\Lambda = 42.0719$.
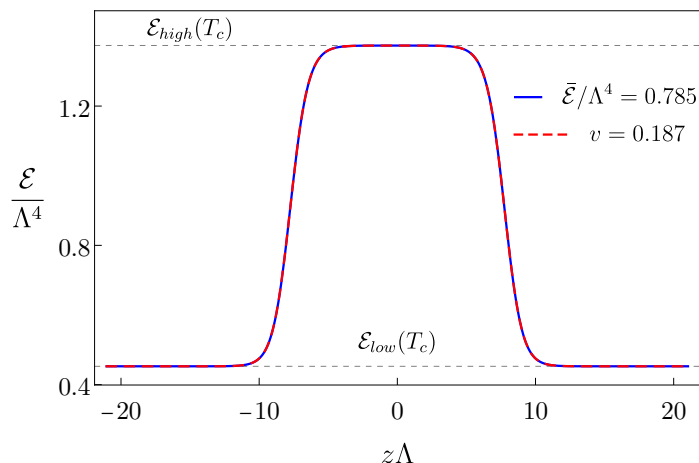

Figure 7: Comparison of the energy profile obtained by Lorentz-transforming the curve in Fig. 6 (dashed, red curve) with a configuration obtained directly as an inhomogeneous, static configuration with the same average energy (3.5) in a box of size $L' = \gamma L$ (solid, blue curve).

The result of applying Eq. (3.4) to the $v = 0.187$ case of Fig. 6 is shown by the dashed, red curve in Fig. 7. As expected, this matches the solid blue curve, corresponding to a profile obtained directly as an inhomogeneous, static configuration with average energy (3.5) in a box of size L'.

We see that, in the case of a single domain, we could have obtained the steady states of Fig. 6 by applying the inverse Lorentz transformation to the corresponding static configurations. In contrast, in the case of two domains moving towards each other that we will consider in the next section, it will be crucial to be able to construct the moving domains via the method described around Eq. (3.1), because in that case we will need to match two baths with opposite velocities.
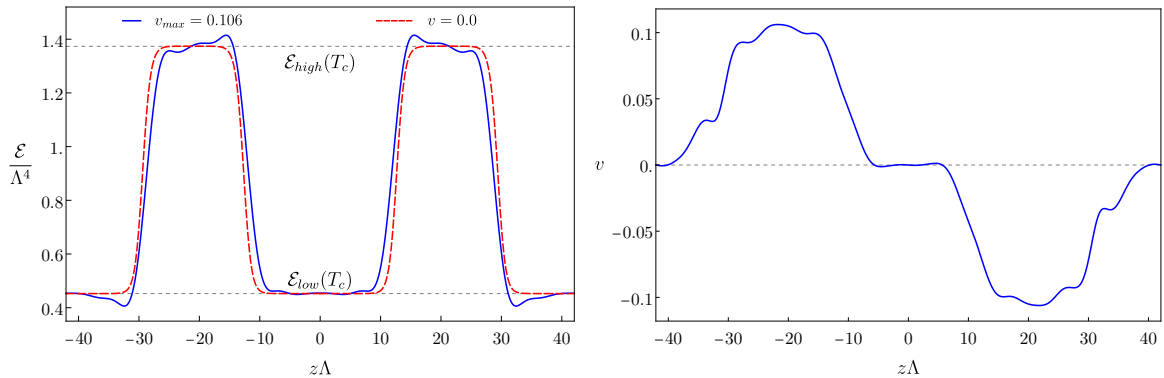
Figure 8: (Left) Initial configuration (dashed red) used to generate two domains in motion (solid blue) that will collide with each other. (Right) Fluid velocity for the domains in motion on the left.

4   Domain collisions

We now turn to the construction of initial states whose evolution will result in the collision of two domains. We start with a configuration consisting of two static domains separated by some distance from one another, like the one described by the dashed, red curve in Fig. 8(left). This can be constructed, for example, by gluing together two individual domains along the low-energy bath. We place the two domains at antipodal points of the z-circle, in which case the resulting configuration is unstable but static [20]. If this configuration is slightly perturbed then, upon time evolution, the domains will approach each other and eventually collide. However, this collision will typically happen at low relative velocity [20]. Therefore, in order to explore the collision physics over a significant range of relative velocities, we will modify the initial configuration following the procedure described around Eq. (3.1). The crucial difference is that now we inject momentum densities of equal magnitudes but opposite signs in each domain. As in the case of a single domain, at the end of the iteration procedure some of the momentum is contained in the bath but most of it is in the domains, as illustrated in Fig. 8(right). Also, the shape of the domains, described by the solid, blue curve in Fig. 8(left), is modified with respect to the static situation. Note that, by symmetry, the fluid velocity must vanish at the two middle points in between the domains, i.e. at $z\Lambda = 0$ and $z\Lambda = L/2$. This is the reason why this initial state cannot be obtained by gluing together two individual steady states of the previous section moving towards each other, since at the middle points the baths would be moving with non-zero, opposite velocities, and hence the velocity field would be discontinuous. One may think that an alternative method would be to use superposition instead of gluing. Specifically, we recall that, in the characteristic formulation that we use on the gravity side (see [21] for details), the data on the initial time slice is free. We can therefore superpose the initial data corresponding to two individual domains moving towards each other. Although this procedure is conceptually sensible, it is technically challenging to find the apparent horizon in the resulting geometry. For this reason we followed the procedure described around Eq. (3.1).

We performed a series of identical simulations except for the fact that we varied the maximum velocity of the fluid in the initial state in the range $v_{\max} \in (0, 0.73)$. We use this velocity as one possible characterization of the initial state. In all cases we fixed the

9

distance between the mid points of the domains to $d\Lambda \simeq 42$. We found three qualitatively different dynamical regimes. For low values $v_{\max} \lesssim v_1 \simeq 0.09$ the domains initially slow down, enter a quasi-static regime, and eventually collide and merge. For intermediate values $v_1 \lesssim v_{\max} \lesssim v_2 \simeq 0.2$ the quasi-static phase is absent. For high values $v_{\max} \gtrsim v_2$ the domains collide but do not merge. Instead they break apart and merge only in subsequent collisions.

We emphasize that there is no sharp transition between these regimes and hence the differences are qualitative in nature. For the specific simulations with the domains of Fig. 8 we found the quoted values $v_1 \simeq 0.09, v_2 \simeq 0.2$. Repeating these simulations for different initial domains we found that the values of v_1, v_2 depend on the choice of initial domains. However, the existence of three qualitatively different regimes persisted, suggesting that it is a robust property of the collision dynamics.

4.1   Low velocity

Fig. 9 shows the evolution of the energy density and the fluid velocity for a simulation with $v_{max} = 0.08$. We can distinguish several stages of the evolution: the initial slowing down of the domains, the quasi-static regime, the merging into a single domain and the subsequent relaxation to equilibrium.

In the first stage, $t\Lambda \lesssim 100$, the domains slow down as they transfer momentum to the low-energy bath in between them. This results in an increase of the energy density and of the longitudinal pressure at the center, as shown at early times in Fig. 10. We use the area density of the apparent horizon on the gravity side as a proxy for the entropy density of the system. As shown in Fig. 11, the dissipation in the initial phase causes a considerable increase in the entropy of the system, meaning that it is comparable to the entropy increase in the final merger.

In the period $100 \lesssim t\Lambda \lesssim 500$ the energy density (the pressure) at the centre increases (decreases) slowly. The quasi-static nature of this regime can be clearly seen in the entropy, which displays a plateau that extends up to $t\Lambda \sim 500$. Note that the entropy of the plateau coincides with that of the initial two-domain configuration (dashed, red curve in Fig. 8(left)), which is static. Presumably, this agreement is due to the fact that the velocity of the two domains in the quasi-static regime is extremely low, as can be seen in Fig. 9(bottom). This is consistent with the fact that the domains move as rigid bodies whose profiles are very well approximated by the equilibrium profile, as shown in Fig. 12(left). The right plot in this figure also shows that the dynamics is driven by a small pressure deficit in the region in between the domains.

The fact that the entropy of the system at times $t\Lambda \lesssim 100$ is lower than the entropy of two static domains means that the procedure by which we inject momentum into the system at constant total energy decreases the entropy. This can be easily understood on the gravity side, where this procedure increases the total momentum of the dual black brane while keeping its mass fixed. If one performs a Kaluza-Klain reduction along the z-direction, this corresponds to increasing the electric charge of the resulting, lower-dimensional black brane while keeping its mass fixed. Just in a Reissner-Nordström black hole, this procedure is expected to reduce the entropy.

The collision takes place around $t\Lambda \sim 500$. The two domains merge into a single, out-of-equilibrium, larger domain that will eventually reach equilibrium through damped oscillations. At sufficiently late times we expect to be able to describe the dynamics in terms of an equilibrium profile plus small deviations, $\delta\mathcal{E}/\mathcal{E} \ll 1$, so that we can apply a linear analysis. Following [20], we model the system at late times as two phases of energies $\mathcal{E}_{low}$ and $\mathcal{E}_{high}$ separated by two interfaces or walls that can move as a whole but whose shapes are rigid.
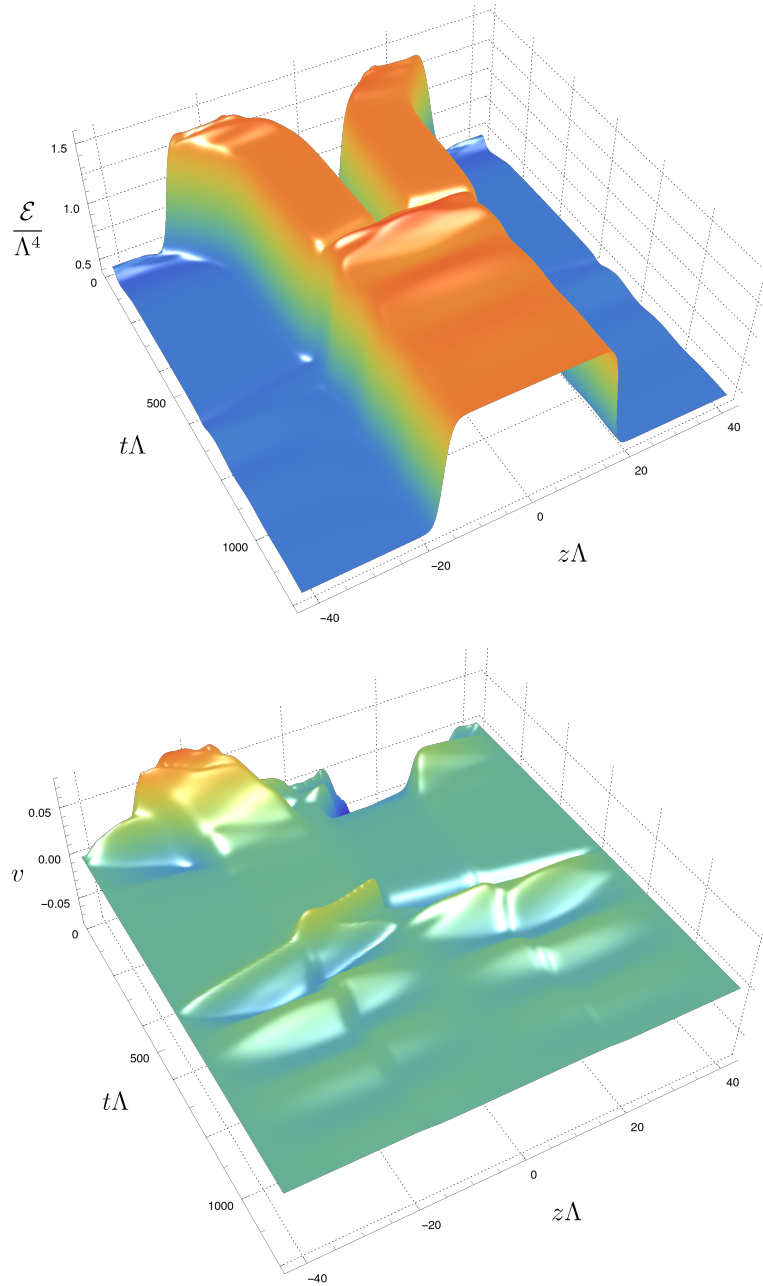
Figure 9: Evolution of the energy density (top) and of the fluid velocity (bottom) for a simulation with $v_{\max} = 0.08$.

Since the system is symmetric under $z \to -z$ we will often focus only on $z > 0$ and speak of "the" wall. We define the positions of the wall as the point at which the energy density is the average between $\mathcal{E}_{high}$ and $\mathcal{E}_{low}$, namely we require that $\mathcal{E}(t, z_{wall}) = (\mathcal{E}_{high} + \mathcal{E}_{low})/2$. The size of the high-energy phase is then $\ell_1 = 2z_{wall}$ and the size of the low-energy phase is $\ell_2 = L - \ell_1$. Rigidity implies that the perturbations of each phase must vanish at the wall, meaning that the only allowed perturbations are odd cosine harmonics of wavelength $\lambda_i = 2\ell_i$. In general there could also be sine harmonic of wavelength $\lambda_i = \ell_i$, but these are excluded in our particular case because of the reflection symmetry. As both subsystems are coupled
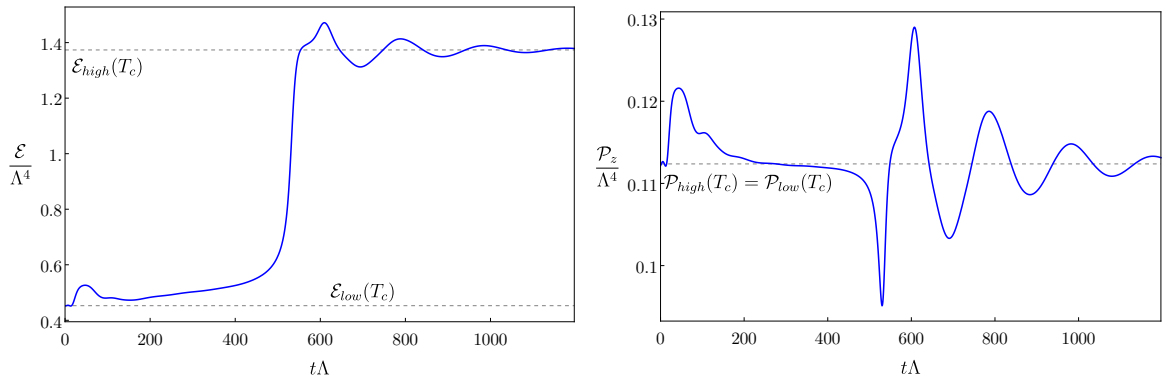
11

Figure 10: Energy density (left) and longitudinal pressure (right) as a function of time at $z\Lambda = 0$ for the collision of Fig. 9.
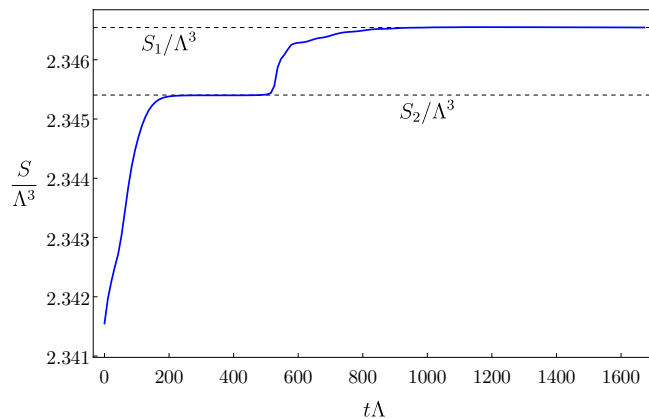

Figure 11: Time evolution of the total entropy (per unit transverse area) for the collision of Fig. 9. S_2 is the entropy of a static configuration with two domains (the dashed, red curve in Fig. 8). S_1 is the entropy of a static configuration with the same total energy but a single domain.

and the wall is rigid we expect the two phases to oscillate in time as a whole, with identical frequencies. Since translation invariance is broken, all the modes in the Fourier decomposition of $\delta\mathcal{E} = \mathcal{E}(t,z) - \mathcal{E}_{eq}(z)$, with $\mathcal{E}_{eq}(z)$ the equilibrium profile at asymptotic times, will mix with one another. Thus, at late times they should all oscillate with the frequency of the longest-lived mode (see Fig. 25 in [29] for a related discussion). We verified this for modes up to $n = 14$, i.e. for modes with momentum up to $k = 14 \times 2\pi/L$. Fig. 13 illustrates the result for the four lowest modes. This result motivates the following ansatz for the perturbations of each phase at late times:

$$\delta\mathcal{E}_i(t,z) = \begin{cases} e^{\omega_1(t-t_0)} \sum_{n=0}^{\infty} a_n^i \cos\left[\omega_2(t-t_0) + \gamma_n^i\right] \cos\left[\frac{(2n+1)\pi}{\ell_i}\left(z - z_0^i\right)\right], & \left|z - z_0^i\right| \leq \frac{\ell_i}{2} \\ 0, & \text{otherwise,} \end{cases}$$

$$(4.1)$$

where the index i refers to each of the two phases and z_0^i refers to their midpoints. The form
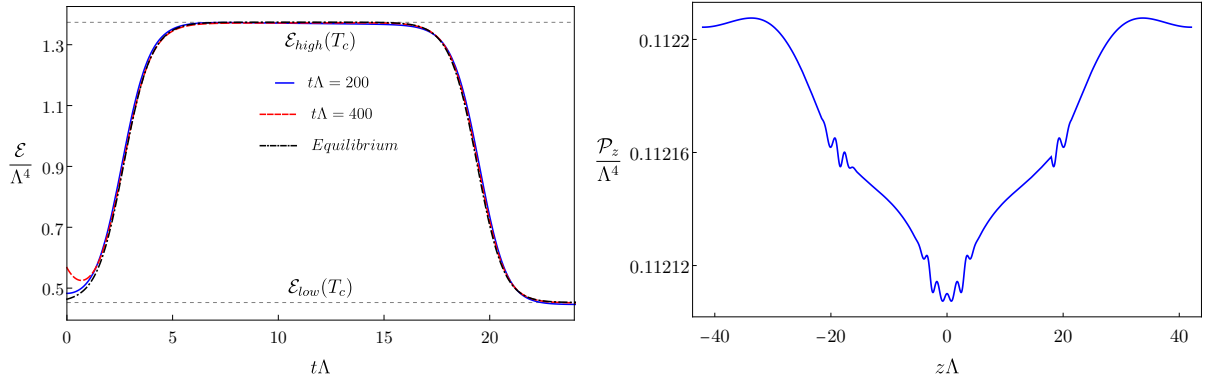
12

Figure 12: (Left) Energy profiles (shifted by an appropriate amount) of the domains during the quasi-static phase for the collision of Fig. 9. (Right) Snapshot of the longitudinal pressure distribution at $t\Lambda = 350$.

of the energy density at late times is then

$$\mathcal{E}(t,z) = \mathcal{E}_{eq}\left(z \mp \frac{\Delta\ell_1(t)}{2}\right) + \delta\mathcal{E}_{high}(t,z) + \delta\mathcal{E}_{low}(t,z), \qquad (4.2)$$

where $\mp$ means that we use $-$ ($+$) if $z > 0$ ($z < 0$). The second and third terms on the right-hand side describe the oscillation in time and space of the two phases. The first term is due to the rigid motion of the walls as the phase domains oscillate. If we call $\Delta\ell_1(t) = -\Delta\ell_2(t)$ the changes in the sizes of the two phases caused by the motion of the walls, then mathematically this means that the oscillations happen on top of phases with sizes $\ell_i + \Delta\ell_i(t)$, whose energy density can be written approximately as the first term in (4.2). The form of this term is just a simple way of "stretching" (for positive $\Delta\ell_i$) or "compressing" (for negative $\Delta\ell_i$) the domain profile by "gluing in" or "cutting out" a small piece at the centre of each phase, taking advantage of the fact that the energy density is almost exactly constant there. In order to determine $\Delta\ell_1$ as a function of time, we simply impose conservation of energy, namely that the energy change associated to the rigid shift of the walls is exactly compensated by the energy change associated to the oscillations of the phases:

$$2\left(\mathcal{E}_{high} - \mathcal{E}_{low}\right)\Delta\ell_1(t) + \int_{-L/2}^{L/2} dz \left[\delta\mathcal{E}_{high}(t,z) + \delta\mathcal{E}_{low}(t,z)\right] = 0. \qquad (4.3)$$

The approximation (4.2) becomes applicable soon after the merger, as illustrated by Fig. 14. To describe correctly the perturbations of the high-energy phase it is enough to truncate the series (4.1) at $n = 1$, whereas in order to obtain a good result for the low-energy phase we included the second mode, $n = 2$. The values that we found for the fit parameters in (4.1) are

$$
\begin{aligned}
\omega_1/\Lambda &= -0.0048, & \omega_2/\Lambda &= 0.032, & t_0\Lambda &= 800, \\
L_{high}\Lambda &= 33.33, & L_{low}\Lambda &= 50.82, & L\Lambda &= 84.14, \\
z_0^{high} &= 0, & z_0^{low} &= \pm L/2, & a_1^{high}/\Lambda^4 &= 0.0375, \\
\gamma_1^{high} &= 0.227, & a_1^{low}/\Lambda^4 &= 0.0142, & \gamma_1^{low} &= 2.346, \\
a_2^{low}/\Lambda^4 &= -0.0022, & \gamma_2^{low} &= -0.244. &
\end{aligned}
\qquad (4.4)
$$

13
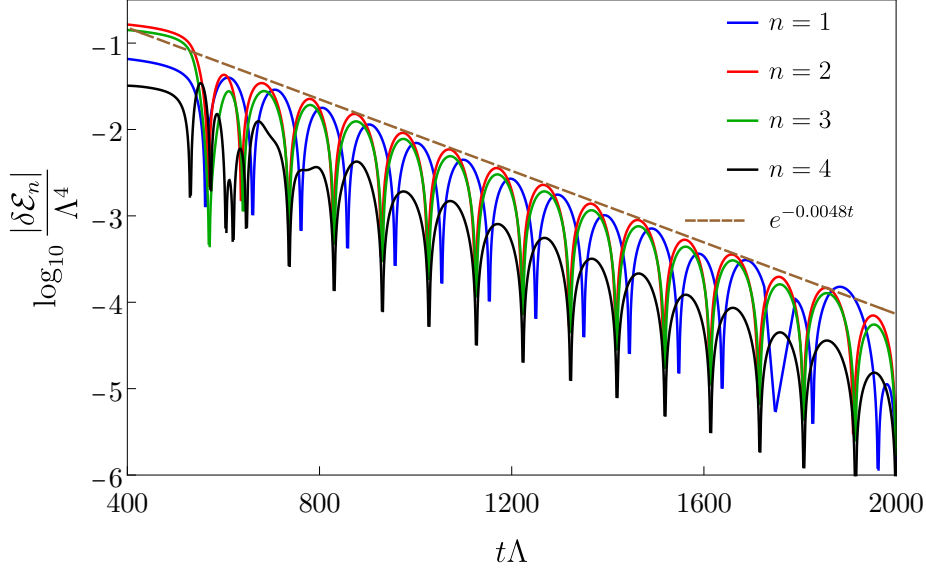
Figure 13: Time evolution of the spatial Fourier modes of $\delta\mathcal{E} = \mathcal{E}(t,z) - \mathcal{E}_{eq}(z)$ after the merging. All modes evolve as $\delta\mathcal{E}_n \sim \exp(\omega_1 t)\cos(\omega_2 t)$ with the same $(\omega_1, \omega_2) = (-0.012, 0.063)$.

4.2 Intermediate velocity

A simulation in this regime with $v_{max} = 0.11$ is shown in Fig. 15. In this case there is no quasi-static regime, as seen by the absence of an intermediate plateau in the entropy density in Fig. 16. The overall increase in the entropy is greater than in the low-velocity case, confirming the intuition that this is a more violent collision. The rest of the evolution is qualitatively similar to the low-velocity case: there is an initial excess of pressure between the domains that slows them down and they merge to form a domain that relaxes to equilibrium through the same kind of oscillations, see Fig. 17. Applying (4.2) leads to a good description of the oscillations at times soon after the collision, see Fig. 18. The parameters in this case are

$$
\begin{aligned}
& \omega_1/\Lambda = -0.0047, && \omega_2/\Lambda = 0.032, && t_0\Lambda = 200, \\
& L_{high}\Lambda = 33.33, && L_{low}\Lambda = 50.82, && L\Lambda = 84.14, \\
& z_0^{high} = 0, && z_0^{low} = \pm L/2, && a_1^{high}/\Lambda^4 = 0.1065, \\
& \gamma_1^{high} = 2.09, && a_1^{low}/\Lambda^4 = -0.0397, && \gamma_1^{low} = 1.306, \\
& a_2^{low}/\Lambda^4 = -0.0082, && \gamma_2^{low} = 1.26\,.
\end{aligned}
\tag{4.5}
$$

Note that, up to fitting errors, the frequencies in this case and in the low-velocity case are the same. The reason is that the final equilibrium state is the same in both cases, and therefore the frequencies of the linear perturbations around it are identical. The only difference between the simulations is therefore in the amplitudes of the oscillations. The following table collects the
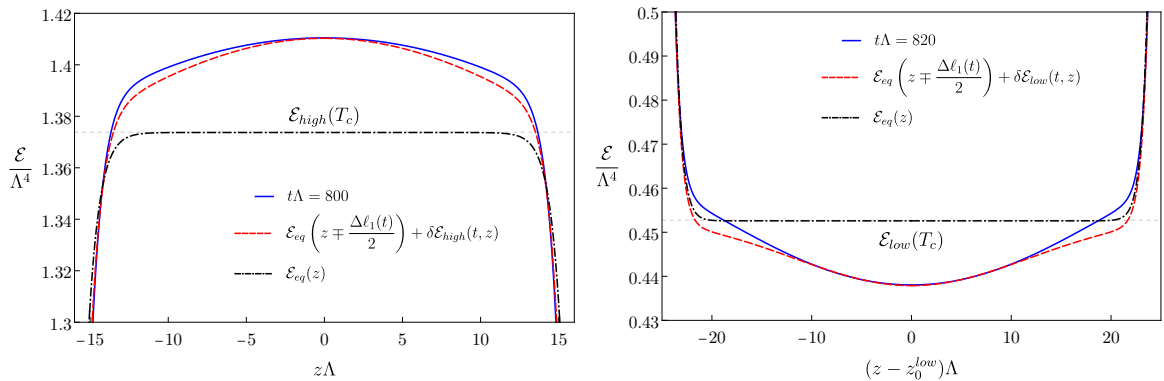
Figure 14: Oscillations of the high- and low-energy phases during the relaxation period after the merger.

ratios of the coefficients for the $n = 1, 2$ modes, a_2^i / a_1^i, for both phases for various simulations:

v_{max}	low	intermediate
low − energy phase	−0.158	0.2058
high − energy phase	−0.043	−0.044

(4.6)

We see that they are of the same order for different simulations, and that the ratio is smaller in the high-energy phase, consistently with our neglect of the $n = 2$ (and higher) modes in this phase.

4.3 High velocity

For velocities $v_{max} \geq v_2 = 0.2$ the domains collide but do not merge in the first collision. Instead, the excited state that results from the collision breaks apart into pieces that will subsequently collide again until they finally merge. Fig. 19 shows two illustrative cases. As shown by Fig. 20, the peak energy density right after the first collision increases significantly with v_{max}, meaning that the resulting configuration is a large deviation from an equilibrium domain. The maximum relative deformations are $\mathcal{E}_{peak} / \mathcal{E}_{high} \simeq 1.071, 1.096, 1.762, 3.966$, respectively, for the increasing velocities shown in Fig. 20. As a consequence, non-linear dynamics becomes important and the excited state breaks apart into smaller components rather than relaxing to a single equilibrium domain as in previous sections.

In both cases shown in Fig. 19, the initial excited state first "emits" perturbations that travel away from the central blob, and subsequently it splits into two fragments. The perturbations travel away from the central blob, colliding with each other on the other side of the box, at $z\Lambda \simeq 42$. We will refer to this as the second collision. This collision creates an excitation that quickly becomes a new domain smaller than the central fragments, as illustrated in Fig. 21. Note from the horizontal axis in this figure that the new domain is shown in the center of the figure and the central fragments on the sides of it. At later times the two central fragments reach the location of the new domain and a third collision, this time a three-body one, takes place. In cases with $v_{max} \gtrsim v_2$, such as the one in Fig. 19(top), this third collision results in the formation of a single domain that then relaxes to equilibrium as described in previous sections.
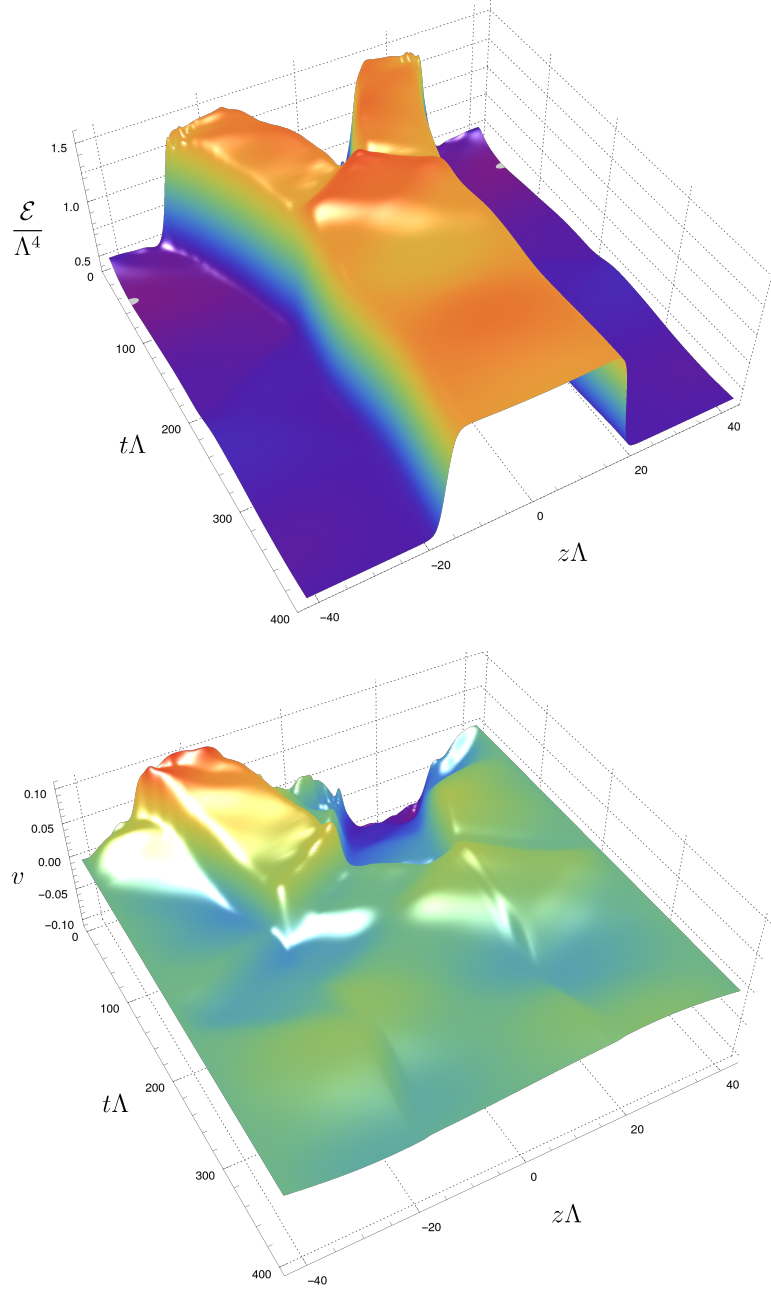
15

Figure 15: Evolution of the energy density (top) and of the fluid velocity (bottom) for a simulation with $v_{\max} = 0.11$.

In contrast, in cases with large enough v_{max}, such as the one of Fig. 19(bottom), the excitations emitted by the initial excited state, as well as the fragments to which it decays, travel faster to the opposite side of the box and do not have time to relax to domains, as shown in Fig. 22(top). As above, the perturbations collide in what we call the second collision. However, in this case the third collision, i.e. the collision between the resulting new structure and the fragments from the first excited state, is again a high-velocity collision. As a consequence, it results in the emission of new perturbations plus fragments that in this case travel from $z\Lambda \simeq 42$ towards $z\Lambda = 0$. These products now have time to relax to approximate domains, as illustrated in Fig. 22(bottom). The perturbations merge in a fourth collision at

16
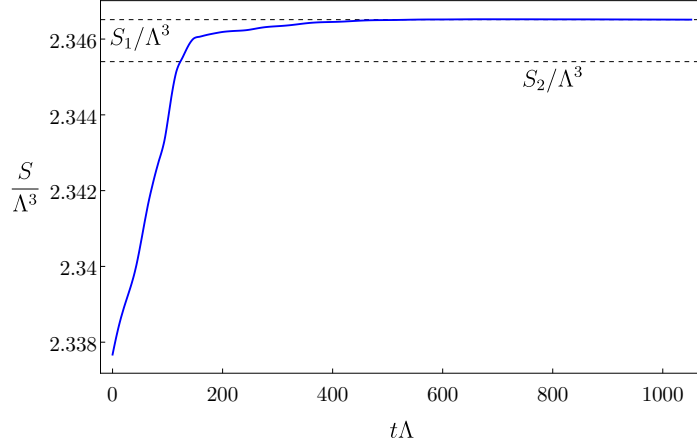
Figure 16: Time evolution of the total entropy (per unit transverse area) for the evolution in Fig. 15. S_2 is the entropy of a static configuration with two domains (the dashed, red curve in Fig. 8). S_1 is the entropy of a static configuration with the same total energy but a single domain.
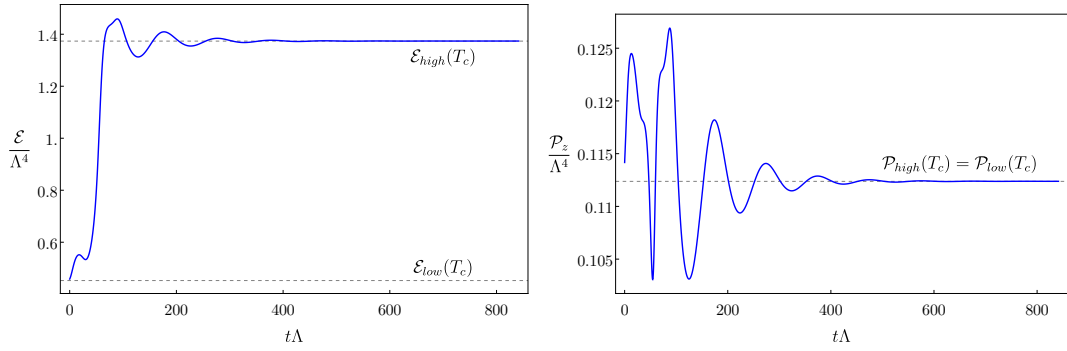

Figure 17: (Left) Energy density $\mathcal{E}/\Lambda^4$ and (Right) longitudinal pressure P_l/Λ^4 as a function of time for constant coordinate $z\Lambda = 0$ for the evolution in Fig. 15.
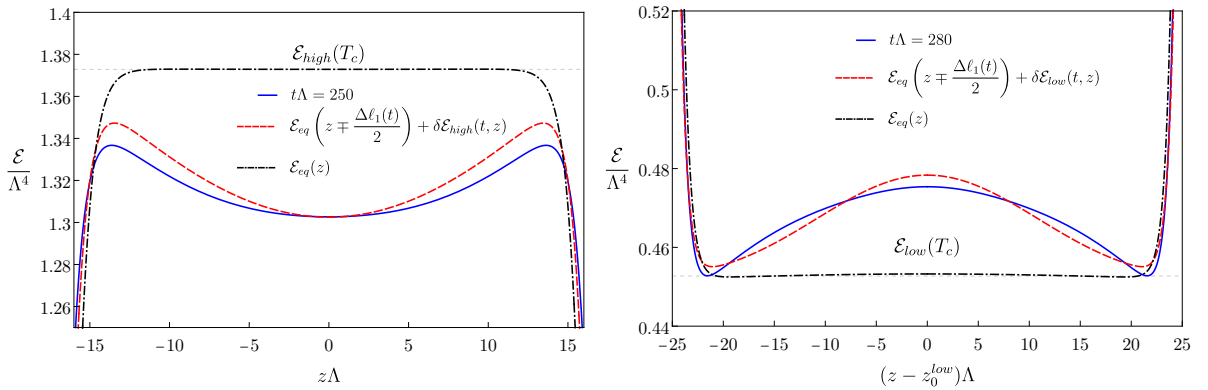

Figure 18: Oscillations of the high- and low-energy phases during the relaxation period after the merger for the evolution in Fig. 15.
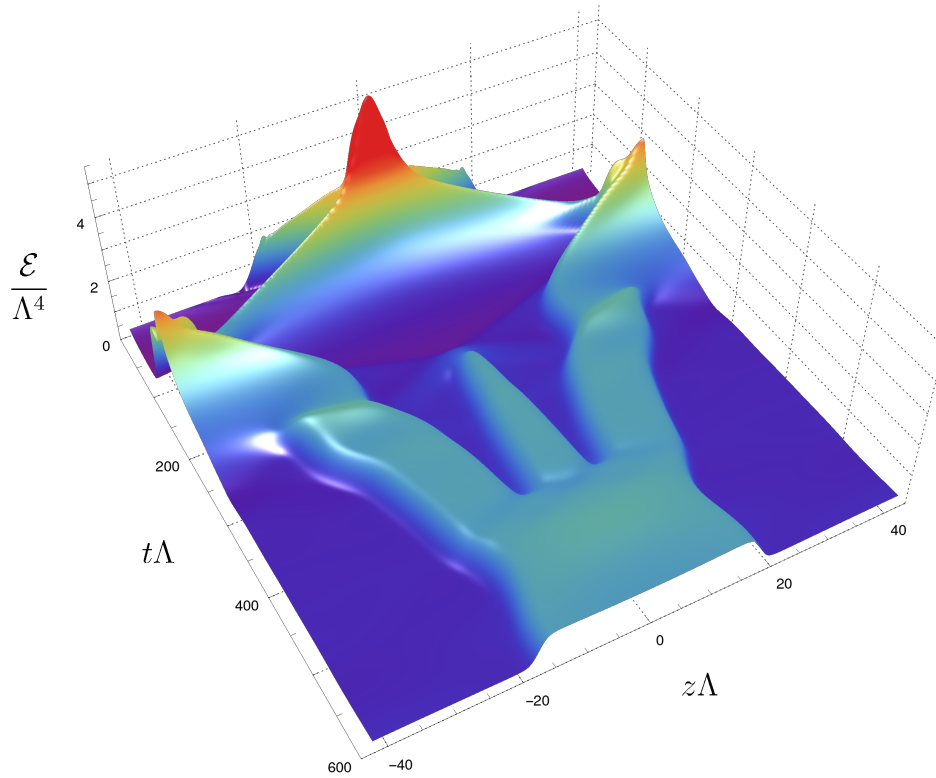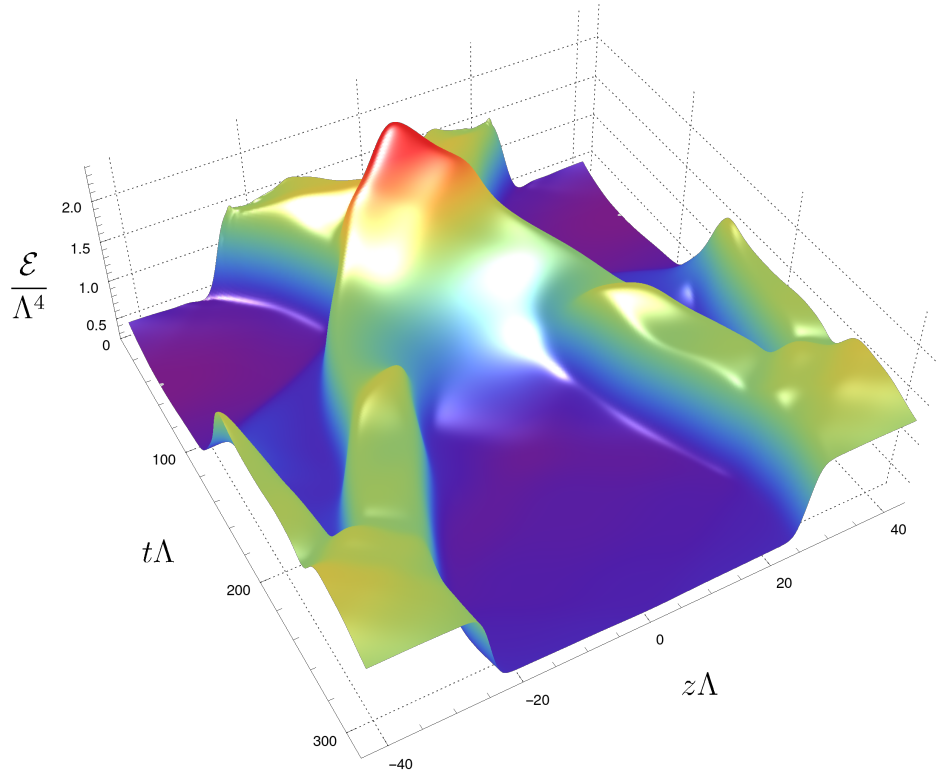
Figure 19: Evolution of the energy density for simulations with $v_{\max} = 0.25$ (top) and $v_{\max} = 0.73$ (bottom).
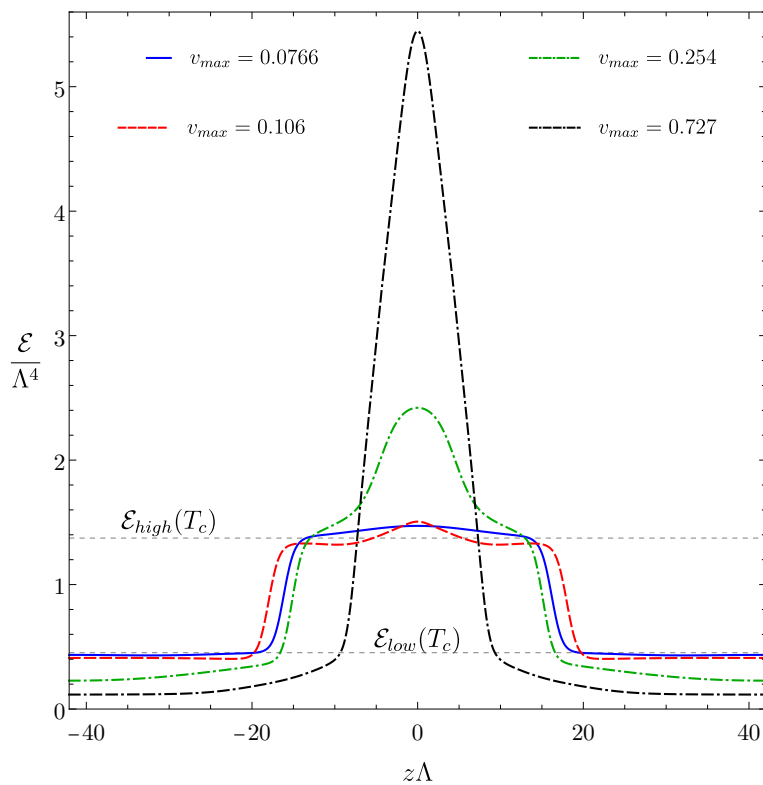
Figure 20: Snapshots of the energy density at the times at which the maximum energy is reached for collisions with different v_{max}.
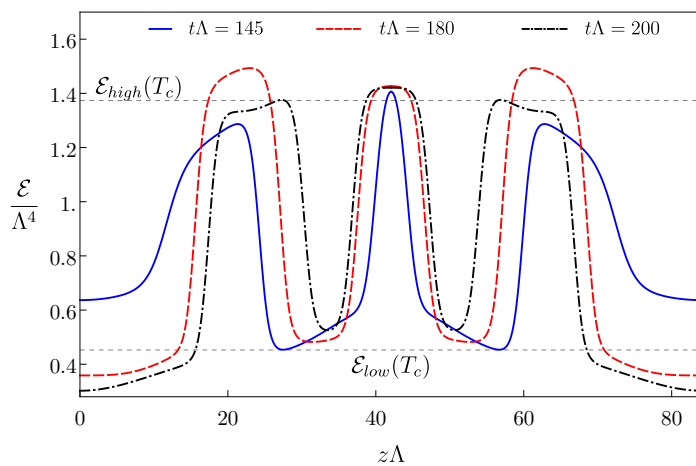

Figure 21: Snapshots of the energy density for the collision of Fig. 19(top) with $v_{max} = 0.25$. The blue curve corresponds to a time soon after the fragmentation of the excited state. Note that the horizontal axis in this figure has been shifted to show the new domain at the center of the figure and the central fragments on the sides of it.

$z\Lambda = 0$, and finally a fifth collision occurs, again a three-body collision, which results in the formation of a single domain that relaxes to equilibrium as in previous sections.
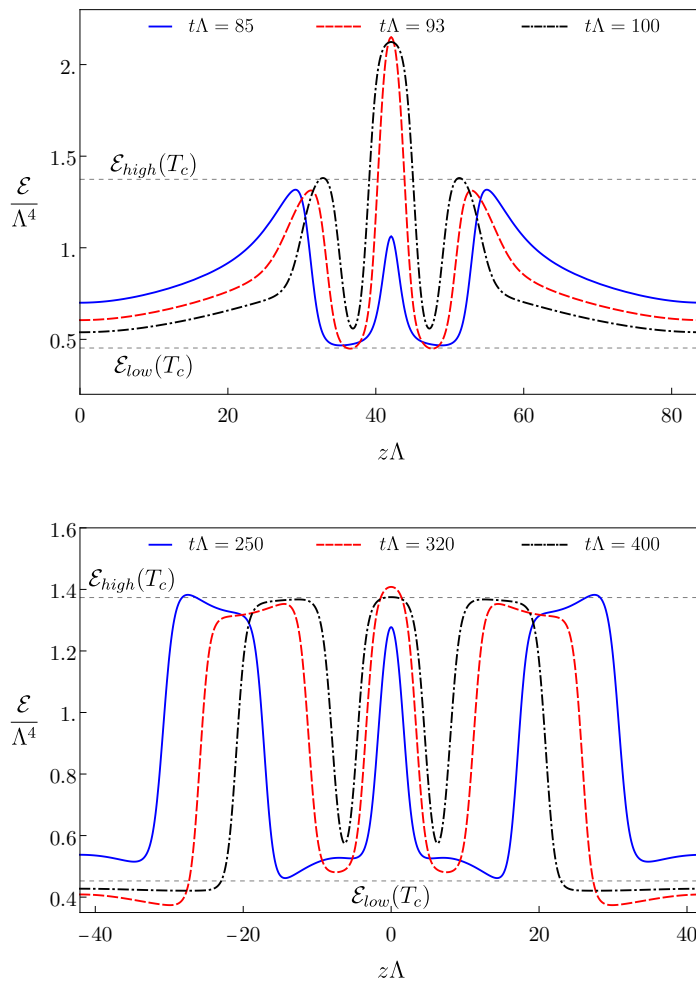
Figure 22:   Snapshots of the energy density for the evolution in Fig. 19(bottom) with $v_{max} = 0.73$. The top (bottom) plot corresponds to a time shortly after the second (fourth) collision. The blue curve corresponds to a time soon after the fragmentation of the excited state.

The entropy production in Fig. 23 reflects the qualitative differences described above between the two evolutions of Fig. 19. On the left plot we can identify three different regimes corresponding to the three different collisions. In contrast, no such clear distinction is apparent on the right plot. In both cases, however, the relative amount of entropy increase is much larger than in the low- and intermediate-velocity collisions. For comparison, the relative entropy production in the evolutions with $v_{max} = 0.11$, $v_{max} = 0.25$ and $v_{max} = 0.73$ are 2, 9 and 45 times larger than in the $v_{max} = 0.08$ case, respectively.

5   Discussion

The time evolution of the spinodal instability in a theory with a first-order phase transition typically results in the creation of phase domains that subsequently collide with one another [20]. The velocities of the different domains are a complicated function of the perturbation of the initial, homogeneous, unstable state. This makes it difficult to perform a systematic study of the physics of the collision as a function of the domain velocities. In this paper
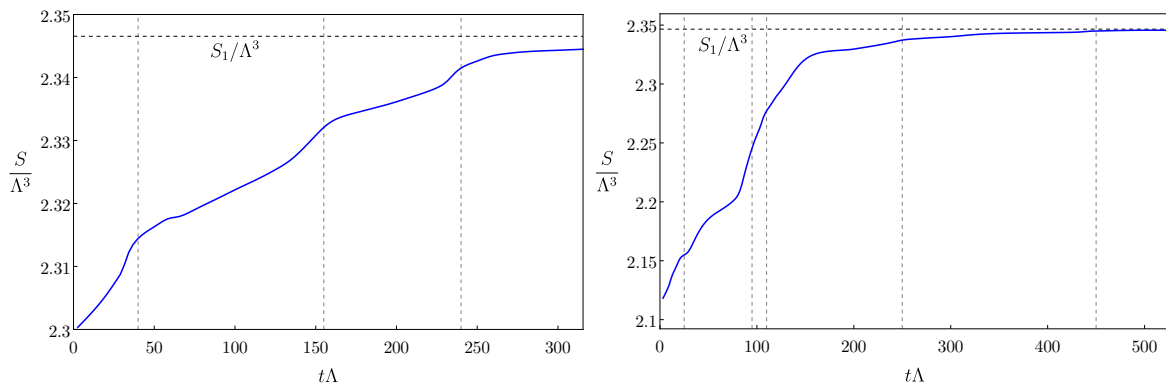
Figure 23: Time evolution of the total entropy (per unit transverse area) for the evolutions of Fig. 19 with $v_{max} = 0.25$ (left) and $v_{max} = 0.73$ (right). S_1 is the entropy of a static configuration with the same total energy but a single domain. The vertical dashed lines represent the approximate time of each collision.

we have overcome this difficulty by directly preparing initial states consisting of domains moving towards each other at velocities $0 \leq v_{max} \leq 0.73$, where v_{max} is the maximum fluid velocity in the initial state. Going to higher velocities becomes challenging due to numerical issues. Nevertheless, the above range sufficed to uncover three qualitatively different dynamical regimes.

For low velocities the domains initially slow down, enter a period of quasi-static evolution, and finally collide and merge into a single domain that then relaxes to equilibrium through damped oscillations. The quasi-static period is clearly visible as a plateau in the entropy of the system, which we computed from the area of the dual horizon on the gravity side. For intermediate velocities the evolution is qualitatively identical except for the fact that no quasi-static period is present. For high velocities the domains can collide several times before they eventually merge into a final, single domain that then relaxes to equilibrium. Our investigations suggest that, while the precise values of the velocities that distinguish these three regimes depend on the size of the domains in question, the existence of these regimes is a robust property of the collision dynamics.

Acknowledgements

References

[1] P. M. Chesler and L. G. Yaffe, "Horizon formation and far-from-equilibrium isotropization in supersymmetric Yang-Mills plasma," Phys. Rev. Lett. **102**, 211601 (2009) doi:10.1103/PhysRevLett.102.211601 [arXiv:0812.2053 [hep-th]].

[2] P. M. Chesler and L. G. Yaffe, "Boost invariant flow, black hole formation, and far-from-equilibrium dynamics in N = 4 supersymmetric Yang-Mills theory," Phys. Rev. D **82**, 026006 (2010) doi:10.1103/PhysRevD.82.026006 [arXiv:0906.4426 [hep-th]].

[3] M. P. Heller, R. A. Janik and P. Witaszczyk, "The characteristics of thermalization of boost-invariant plasma from holography," Phys. Rev. Lett. **108**, 201602 (2012) doi:10.1103/PhysRevLett.108.201602 [arXiv:1103.3452 [hep-th]].

[4] P. M. Chesler and L. G. Yaffe, "Holography and colliding gravitational shock waves in asymptotically AdS$_5$ spacetime," Phys. Rev. Lett. **106**, 021601 (2011) doi:10.1103/PhysRevLett.106.021601 [arXiv:1011.3562 [hep-th]].

[5] M. P. Heller, D. Mateos, W. van der Schee and D. Trancanelli, "Strong Coupling Isotropization of Non-Abelian Plasmas Simplified," Phys. Rev. Lett. **108**, 191601 (2012) doi:10.1103/PhysRevLett.108.191601 [arXiv:1202.0981 [hep-th]].

[6] M. P. Heller, D. Mateos, W. van der Schee and M. Triana, "Holographic isotropization linearized," JHEP **1309**, 026 (2013) doi:10.1007/JHEP09(2013)026 [arXiv:1304.5172 [hep-th]].

[7] J. Casalderrey-Solana, M. P. Heller, D. Mateos and W. van der Schee, "From full stopping to transparency in a holographic model of heavy ion collisions," Phys. Rev. Lett. **111**, 181601 (2013) [arXiv:1305.4919 [hep-th]].

[8] J. Casalderrey-Solana, M. P. Heller, D. Mateos and W. van der Schee, "Longitudinal Coherence in a Holographic Model of Asymmetric Collisions," Phys. Rev. Lett. **112**, no. 22, 221602 (2014) [arXiv:1312.2956 [hep-th]].

[9] P. M. Chesler and L. G. Yaffe, "Holography and off-center collisions of localized shock waves," JHEP **1510**, 070 (2015) [arXiv:1501.04644 [hep-th]].

[10] P. M. Chesler, "Colliding shock waves and hydrodynamics in small systems," Phys. Rev. Lett. **115**, no. 24, 241602 (2015) [arXiv:1506.02209 [hep-th]].

[11] P. M. Chesler and W. van der Schee, "Early thermalization, hydrodynamics and energy loss in AdS/CFT," Int. J. Mod. Phys. E **24**, no. 10, 1530011 (2015) [arXiv:1501.04952 [nucl-th]].

[12] A. Buchel, M. P. Heller and R. C. Myers, "Equilibration rates in a strongly coupled nonconformal quark-gluon plasma," Phys. Rev. Lett. **114** (2015) no.25, 251601 [arXiv:1503.07114 [hep-th]].

[13] P. M. Chesler, "How big are the smallest drops of quark-gluon plasma?," JHEP **1603**, 146 (2016) [arXiv:1601.01583 [hep-th]].

[14] M. Attems, J. Casalderrey-Solana, D. Mateos, D. Santos-Oliván, C. F. Sopuerta, M. Triana and M. Zilhão, "Holographic Collisions in Non-conformal Theories," JHEP **1701**, 026 (2017) [arXiv:1604.06439 [hep-th]].

[15] J. Casalderrey-Solana, D. Mateos, W. van der Schee and M. Triana, "Holographic heavy ion collisions with baryon charge," JHEP **1609**, 108 (2016) doi:10.1007/JHEP09(2016)108 [arXiv:1607.05273 [hep-th]].

[16] M. Attems, J. Casalderrey-Solana, D. Mateos, I. Papadimitriou, D. Santos-Oliván, C. F. Sopuerta, M. Triana and M. Zilhão, "Thermodynamics, transport and relaxation in non-conformal theories," JHEP **1610**, 155 (2016) [arXiv:1603.01254 [hep-th]].

[17] U. Gürsoy, A. Jansen and W. van der Schee, "New dynamical instability in asymptotically anti-de Sitter spacetime," Phys. Rev. D **94**, no. 6, 061901 (2016) [arXiv:1603.07724 [hep-th]].

[18] M. Attems, Y. Bea, J. Casalderrey-Solana, D. Mateos, M. Triana and M. Zilhao, "Phase Transitions, Inhomogeneous Horizons and Second-Order Hydrodynamics," JHEP **1706**, 129 (2017) [arXiv:1703.02948 [hep-th]].

[19] R. A. Janik, J. Jankowski and H. Soltanpanahi, "Real-Time dynamics and phase separation in a holographic first order phase transition," Phys. Rev. Lett. **119**, no. 26, 261601 (2017) [arXiv:1704.05387 [hep-th]].

[20] M. Attems, Y. Bea, J. Casalderrey-Solana, D. Mateos and M. Zilhão, "Dynamics of Phase Separation from Holography," JHEP **01** (2020), 106 [arXiv:1905.12544 [hep-th]].

[21] M. Attems, J. Casalderrey-Solana, D. Mateos, D. Santos-Oliván, C. F. Sopuerta, M. Triana and M. Zilhão, "Paths to equilibrium in non-conformal collisions," JHEP **1706**, 154 (2017) [arXiv:1703.09681 [hep-th]].

[22] R. Rougemont, R. Critelli, J. Noronha-Hostler, J. Noronha and C. Ratti, "Dynamical versus equilibrium properties of the QCD phase transition: A holographic perspective," Phys. Rev. D **96** (2017) no.1, 014032 [arXiv:1704.05558 [hep-ph]].

[23] R. Critelli, R. Rougemont and J. Noronha, "Holographic Bjorken flow of a hot and dense fluid in the vicinity of a critical point," Phys. Rev. D **99**, no. 6, 066004 (2019) doi:10.1103/PhysRevD.99.066004 [arXiv:1805.00882 [hep-th]].

[24] A. Buchel, "Non-conformal holographic Gauss-Bonnet hydrodynamics," JHEP **1803**, 037 (2018) [arXiv:1801.06165 [hep-th]].

[25] A. Czajka, K. Dasgupta, C. Gale, S. Jeon, A. Misra, M. Richard and K. Sil, "Bulk Viscosity at Extreme Limits: From Kinetic Theory to Strings," JHEP **07** (2019), 145 [arXiv:1807.04713 [hep-th]].

[26] A. Czajka, K. Dasgupta, C. Gale, S. Jeon, A. Misra, M. Richard and K. Sil, "On bulk viscosity at weak and strong 't Hooft couplings," Mod. Phys. Lett. A **35** (2020) no.27, 2030012 [arXiv:1807.07950 [hep-th]].

[27] M. Attems, Y. Bea, J. Casalderrey-Solana, D. Mateos, M. Triana and M. Zilhão, "Holographic Collisions across a Phase Transition," Phys. Rev. Lett. **121**, no. 26, 261601 (2018) doi:10.1103/PhysRevLett.121.261601 [arXiv:1807.05175 [hep-th]].

[28] H. Bantilan, P. Figueras and D. Mateos, "Real-time Dynamics of Plasma Balls from Holography," Phys. Rev. Lett. **124** (2020) no.19, 191601 [arXiv:2001.05476 [hep-th]].

[29] Y. Bea, O. J. C. Dias, T. Giannakopoulos, D. Mateos, M. Sanchez-Garitaonandia, J. E. Santos and M. Zilhao, "Crossing a large-N phase transition at finite volume," JHEP **02** (2021), 061 [arXiv:2007.06467 [hep-th]].

[30] J. Casalderrey-Solana, C. Ecker, D. Mateos and W. Van Der Schee, "Strong-coupling dynamics and entanglement in de Sitter space," JHEP **03** (2021), 181 [arXiv:2011.08194 [hep-th]].

[31] Y. Bea, J. Casalderrey-Solana, T. Giannakopoulos, D. Mateos, M. Sanchez-Garitaonandia and M. Zilhão, "Bubble Wall Velocity from Holography," [arXiv:2104.05708 [hep-th]].

[32] C. Ecker, W. van der Schee, D. Mateos and J. Casalderrey-Solana, "Holographic Evolution with Dynamical Boundary Gravity," [arXiv:2109.10355 [hep-th]].

[33] J. Casalderrey-Solana, H. Liu, D. Mateos, K. Rajagopal and U. A. Wiedemann, "Gauge/String Duality, Hot QCD and Heavy Ion Collisions," book:Gauge/String Duality, Hot QCD and Heavy Ion Collisions. Cambridge, UK: Cambridge University Press, 2014 [arXiv:1101.0618 [hep-th]].

[34] M. A. Stephanov, K. Rajagopal and E. V. Shuryak, "Signatures of the tricritical point in QCD," Phys. Rev. Lett. **81**, 4816 (1998) [hep-ph/9806219].

[35] M. A. Stephanov, K. Rajagopal and E. V. Shuryak, "Event-by-event fluctuations in heavy ion collisions and the QCD critical point," Phys. Rev. D **60**, 114028 (1999) [hep-ph/9903292].

[36] M. Stephanov and Y. Yin, "Hydrodynamics with parametric slowing down and fluctuations near the critical point," Phys. Rev. D **98** (2018) no.3, 036006 ['arXiv:1712.10305 [nucl-th]].

[37] Y. Bea and D. Mateos, "Heating up Exotic RG Flows with Holography," JHEP **1808** (2018) 034, arXiv:1805.01806 [hep-th].